ACS OMEGA

http://pubs.acs.org/journal/acsodf

Article

Evaluation of the Fault Activation Risk Induced by Hot Dry Rock Reservoir Development Based on Thermal−Hydraulic−Mechanical Coupling

Kai Zhao,* Xiaoyun Wang, Yongcun Feng, Wei Gao, Wenjie Song, Liangbin Dou, and Hailong Jiang

Cite This: *ACS Omega* 2023, 8, 8078−8091

Read Online

ACCESS | Metrics & More | Article Recommendations

ABSTRACT: Due to the nature of hot dry rock resources and the particularity of the development methods, the fault activation induced by injection and production of hot dry rocks involves a complex multifield coupling mechanism. Traditional methods cannot effectively evaluate the fault activation behavior in hot dry rock injection and production. Aiming at the above-mentioned problems, a thermal−hydraulic−mechanical coupling mathematical model of injection and production of hot dry rocks is established and solved by a finite element method. At the same time, the fault slip potential (FSP) is introduced to quantitatively evaluate the risk of fault activation induced by injection and production of hot dry rocks under different injection and production conditions and geological conditions. The results show that under the same geological conditions, the greater the well spacing of injection and production wells, the greater the risk of fault activation induced by injection and production and the greater the injection flow, the greater the risk of fault activation. Under the same geological conditions, the lower the reservoir permeability, the greater the fault activation risk and the higher the initial reservoir temperature, the greater the fault activation risk. Different fault occurrences result in different risks of fault activation. These results provide a certain theoretical reference for the safe and efficient development of hot dry rock reservoirs.

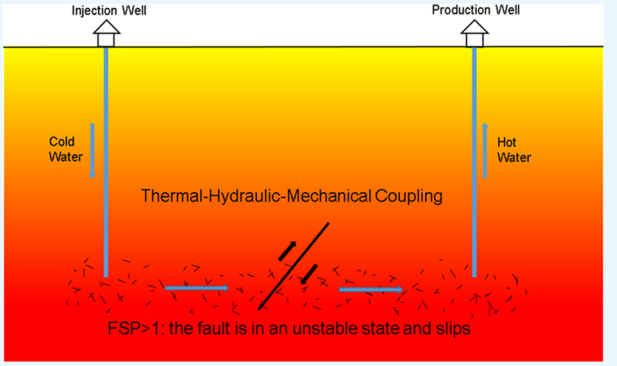

1. INTRODUCTION

In recent years, the contradiction between the international energy supply and demand has gradually increased. Traditional underground energy sources such as coal, oil, and natural gas make it difficult to meet the requirements of future human development in terms of resource surplus and environmental protection. Geothermal resources, as a clean and renewable energy, have gradually become an emerging alternative energy source.[1−3] The hot dry rock system is the most potential and valuable part of geothermal energy, with a buried depth of 2−6 km, temperature of 150−650 °C, and no water or steam.[4,5]However, in recent years, seismic activity has occurred from time to time in the development of hot dry rocks, which resulted in some important geothermal projects to be terminated. According to statistics, since the 1970s, at least 33 of the 79 hot dry rock development projects worldwide have induced earthquakes of greater than 2.0 matrix magnitude (Mw), with the largest magnitude being 5.4 matrix magnitude (Mw) induced by the Pohang hot dry rock project in South Korea.[4−11]

In the past few decades, extensive research has been conducted on the mechanical behavior of faults and many achievements have been applied to the development of underground resources. It is generally believed that fluid injection will lead to an increase in pore pressure and a decrease in the positive pressure at the fault plane, while fluid production will lead to a nonuniform change in ground stress and increase the shear force at the fault plane. Both fluid injection and production will cause fault slips under certain conditions, thus inducing earthquakes. Hubbert et al. studied the influence of the injected fluid on fault stability and pointed out that when the injected fluid pressure is high enough, faults will be reactivated regardless of the occurrence of faults.[12] Raleigh believed that fault failure followed the Moore−Coulomb shear failure criterion because fluid injection would increase the reservoir pore pressure, reduce the positive pressure on the fault surface, and cause fault slippage. In particular the injected fluid volume and pressure, if the deposit of a certain scale fault has suitable fluid mechanics character-

Received: December 23, 2022
Accepted: February 1, 2023
Published: February 14, 2023

https://doi.org/10.1021/acsomega.2c08111
ACS Omega 2023, 8, 8078−8091

istics, stress the connection area of thousands of meters can be formed, as shown in the Denver and Ohio case, induced earthquake analysis of measured in situ stress direction and in situ area direction with good correlation, the seismic activity mainly comes from the first fault activation.[13,14] Nicholson et al. found that deep well injection often induces seismic activity in unstable areas, where existing faults are often present. When the pressure difference is kept constant, the injection pressure offsets part of the confining pressure and axial pressure, reduces the friction between fault discs, and leads to fracture failure or activation of the existing faults.[15] Grasso et al. showed that oil and gas production would not only cause pore pressure attenuation but also cause reservoir compaction deformation, induce nonuniform changes in ground stress, increase shear force at the fault plane, cause the molar circle radius to increase, gradually approach the failure line, and induce fault activation and seismic activity.[16] Segall et al. showed that the generation of pore pressure and temperature-induced stress in the process of geothermal recovery would cause the stress state on the fault to gradually approach the Coulomb failure line and induce a fault slip and seismic activity.[17] Castillo et al. proposed a CFF model without considering fault cohesion. This model can quantitatively describe the minimum fluid pressure required for fault activation and the minimum shear stress during fault activation.[18,19]Evans et al. and Zoback et al. studied the seismic activity caused by CO_2 sequestration under large-scale conditions.[20,21] Zhao studied the fault behavior during the development of depleted reservoirs and concluded that under certain geological conditions, oil and gas production would also cause shear slip on reverse faults, which mainly depended on the initial in situ stress direction, pore pressure, reservoir elastic parameters, fault occurrence, and reservoir recovery degree.[22]

It can be seen that the research object of seismicity induced by injection and production in the above-mentioned research is mainly oil and gas reservoirs, mainly including the seismicity induced by fluid injection and oil flooding, fracturing stimulation, CO_2 sequestration, oil and gas extraction, and other operations, and lots of beneficial understanding and achievements have been achieved.[6,22−24] However, the mechanism of fault activity induced by hot dry rock development is more complex due to the special nature of the hot dry rock and the development operation mode. The existing methods cannot effectively explain the specific reasons for fault activation, which seriously restricts the safe and efficient development of hot dry rock reservoirs.

2. METHODOLOGY

2.1. Thermal−Hydraulic−Mechanical Coupling Mechanism. The hot dry rock reservoir injection and production process involves solid deformation, fluid seepage, and heat conduction between the fluid and solid.[25] In this process, the interaction of the temperature field, seepage field, and deformation field is a complex multifield coupling process, and the multifield coupling relationship is shown in Figure 1.

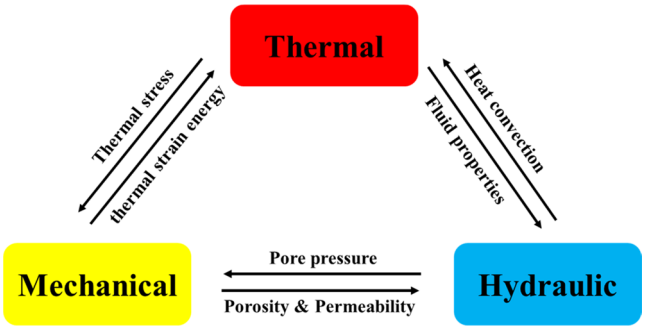

Figure 1. Thermal−hydraulic−mechanical coupling relationship diagram.

(1) Influence of the seepage field on the temperature field: after a low-temperature fluid is injected into the hot dry rock reservoir, intense heat exchange occurs, resulting in a lower reservoir rock temperature and change of the heat balance state under initial conditions.

(2) Influence of the temperature field on the seepage field: after the injected fluid is heated by the high-temperature reservoir, the physical characteristics of seepage, such as viscosity and density of water, change with temperature, affecting the seepage state of the fluid in the rock.

(3) Influence of the temperature field on the strain field: after the injection of a cryogenic fluid into the hot dry rock reservoir, the temperature decreases and thermal strain is generated, and the strain field that remains in balance under the initial in situ stress changes, leading to the response change of reservoir in situ stress.

(4) Influence of the strain field on the temperature field: the deformation of the reservoir produces thermal strain energy, and the deformation of the reservoir will affect the thermal conductivity of the pore structure.

(5) Effect of the seepage field on the strain field: after fluid injection, the pore pressure increases and effective stress in the reservoir decreases.

(6) Effect of the strain field on the seepage field: Deformation leads to changes in the reservoir pore structure and then changes the permeability of the hot dry rock reservoir.

2.2. Governing Equations. To facilitate numerical calculations, certain assumptions need to be made in the theoretical derivation. On the existing research basis, this paper summarizes and makes the following assumptions:

(1) The hot dry rock reservoir is a homogeneous and isotropic linear elastic body, and heat transfer parameters do not change with temperature.

(2) The flow of the fluid in the hot dry rock reservoir follows Darcy's law.

(3) The heat conduction process obeys Fourier's law, regardless of the influence of heat radiation.

(4) The skeleton deformation law of the hot dry rock reservoir obeys the Terzaghi effective stress law.

(5) There is only heat exchange between the fluid and rock, and no chemical reaction occurs.

(6) There is no phase transition, and the fluid flow in the reservoir is a single-phase liquid flow.

2.2.1. Governing Equation of the Stress Field. The force balance equation of the hot dry rock reservoir is

$$\sigma_{ji,j} + F_i = 0 \quad (1)$$

where $\sigma_{ji,j}$ is the stress tensor component, Pa.

According to hypothesis (1), the geometric equation can be expressed in the tensor form as

https://doi.org/10.1021/acsomega.2c08111
ACS Omega 2023, 8, 8078−8091

$$\varepsilon_{ij} = \varepsilon_{ji} = \frac{1}{2}(u_{i,j} + u_{j,i}) \tag{2}$$

where ε_{ij} is the strain tensor component and $u_{i,j}$ is the displacement vector, m.

The constitutive equation (also known as the physical equation) of hot dry rock mass is an equation describing the relationship between stress and strain of rock mass, which can be expressed in the form of tensor

$$\sigma_{ij} = 2G\varepsilon_{ij} + \lambda\delta_{ij}\varepsilon_v \tag{3}$$

where $G = E/2(1 + \nu)$ is the modulus of rigidity, Pa; $\lambda = \frac{E\nu}{(1+\nu)(1-2\nu)}$ is Lamé's constants, Pa; E is the elastic modulus, Pa; ν is Poisson's ratio of rock; and ε_v is the volume strain of the rock.

Considering the thermal expansion of the rock caused by the change of rock temperature, the constitutive equation can be expressed as

$$\sigma_{ij} = 2G\varepsilon_{ij} + \lambda\delta_{ij}\varepsilon_v + 3K\alpha_T(T - T_0) \tag{4}$$

where K is the bulk elastic modulus, Pa; α_T is the thermal expansion coefficient of the rock, 1/K; T is the reservoir temperature, K; and T_0 is the initial reservoir temperature, K.

The governing equation of the stress field under the influence of the temperature field and seepage field can be obtained as

$$Gu_{i,jj} + \frac{G}{1-2\nu}u_{j,ji} - \alpha_p p_{,i} - 3K\alpha_T T_{,i} + F_i = 0 \tag{5}$$

2.2.2. Governing Equation of the Seepage Field. According to the law of mass conservation, the continuity equation of the fluid flow in the rock can be expressed as

$$\frac{\partial(\rho_l\phi)}{\partial t} + \nabla\cdot(\rho_l v) = 0 \tag{6}$$

where ρ_l is the density of the injected fluid density, kg/m^3, and v is the velocity of fluid flow, m/s.

According to the Forchheimer relation $v = \phi v_r$, Darcy's law can be rewritten as

$$\phi v_r = -\frac{k}{\mu}(\nabla p + \rho_l g\nabla z) \tag{7}$$

where v_r is the relative velocity of the fluid flow, m/s; ϕ is the porosity of the rock; k is the permeability of the rock, m^2; μ is the viscosity of the injected fluid, Pa·s; ρ_l is the density of the injected fluid, kg/m^3; and g is the gravitational acceleration, m/s^2.

In the continuity equation, v is the absolute velocity of the fluid flow, so $v_r = v - v_s$. It was fitted into the continuity equation and combined with eq 7. After expansion, we get

$$\phi\frac{\partial\rho_l}{\partial t} + \rho_l\frac{\partial\phi}{\partial t} + \rho_l\phi\nabla\cdot v_s = \nabla\cdot\left(\rho_l\frac{k}{\mu}(\nabla p + \rho_l g\nabla z)\right) \tag{8}$$

where v_s is the viscosity of the rock, m/s.

Considering that the hot dry rock reservoir is hard granite, the rock density is considered to be constant, so the continuity equation of the rock can be written as[26]

$$\frac{\partial(1-\phi)}{\partial t} + \nabla\cdot[(1-\phi)v_s] = 0 \tag{9}$$

Substitute eq 9 into eq 8 to obtain

$$\phi\frac{\partial\rho_l}{\partial t} + \rho_l\nabla\cdot v_s = \nabla\cdot\left(\rho_l\frac{k}{\mu}(\nabla p + \rho_l g\nabla z)\right) \tag{10}$$

In eq 10, ∇v_s can be expressed as

$$\nabla\cdot v_s = \frac{\partial}{\partial t}(\nabla\cdot u_s) = \frac{\partial}{\partial t}(\delta_{ij}\varepsilon_{ij}) = \frac{\partial\varepsilon_V}{\partial t} \tag{11}$$

Under the influence of temperature and pressure, the injected fluid density can be expressed as

$$\rho_l = \rho_{l0}(1 + c_l\Delta p - \beta_l\Delta T) \tag{12}$$

where ρ_{l0} is the initial density of the injected fluid, kg/m^3; c_l is the pressure coefficient of the injected fluid, 1/Pa; and β_l is the temperature coefficient of the injected fluid, 1/K.

Combining eqs 10−12, the governing equation of the seepage field expressed by pressure, temperature, and volume strain can be obtained, as shown in eq 13

$$\phi\rho_0 c_l\frac{\partial p}{\partial t} - \phi\rho_0\beta_l\frac{\partial T}{\partial t} + \rho_l\frac{\partial\varepsilon_V}{\partial t} = \nabla\cdot\left[\rho_l\frac{k}{\mu}(\nabla p + \rho_l g\nabla z)\right] \tag{13}$$

2.2.3. Governing Equation of the Temperature Field. In the process of hot dry rock reservoir development, the low-temperature fluid injected into the reservoir has a strong heat exchange with the hot dry rock mass. The heat exchange between the fluid and the solid follows Fourier's law, and the basic expression is shown in eq 14

$$q = -\lambda\nabla T = -\lambda\frac{\partial T}{\partial n}n \tag{14}$$

where q is the heat flux, J/(s·m^2), and λ is the thermal conductivity of the rock, W/(m·K).

When considering fluid seepage, Fourier's law can be rewritten as

$$q = -\lambda\nabla T + c_f\rho_l T v \tag{15}$$

According to the law of conservation of energy, the net heat flow into the control body + the heat generated by the heat source in the control body = the increase of the internal energy of substances in the control body

$$\frac{\partial}{\partial t}(c_s\rho_s T) = \nabla\cdot(-\nabla q) + q_V \tag{16}$$

where c_s is the specific heat capacity of rock, J/(kg·°C), and ρ_s is the density of rock, kg/m^3.

The calorific value of the heat source in the rock is affected by the joint action of fluid seepage and solid, and the influence of the seepage is expressed in eq 15. The heat generated by the rock deformation is

$$(1-\phi)\alpha_T T\frac{\partial\varepsilon_v}{\partial t} \tag{17}$$

According to eqs 15−17, the controlling equation of the temperature field under the action of fluid seepage and rock deformation can be obtained as follows

$$\frac{\partial}{\partial t}[(\phi\rho_l c_l + (1-\phi)\rho_s c_s)T] = \lambda\nabla^2 T + c_f\rho_l[v\cdot\nabla T + T\nabla\cdot v] + (1-\phi)\alpha_T T\frac{\partial\varepsilon_v}{\partial t} \tag{18}$$

https://doi.org/10.1021/acsomega.2c08111
ACS Omega 2023, 8, 8078−8091

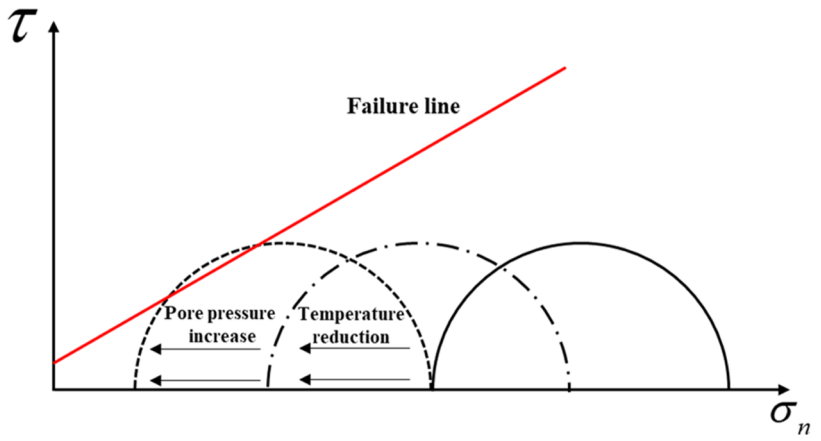

Figure 2. Effect of pore pressure and thermal stress increase on fault stability.

where c_f is the specific heat capacity of the injected fluid, J/(kg·°C).

The above-mentioned equations include fluid seepage, solid deformation, and temperature change, which need to be solved together with the governing equation of seepage field and the governing equation of stress field.

2.3. Fault Slip Mechanical Mechanism. The generation of the fault slip is controlled by the stress state on the fault surface. The Coulomb failure criterion can be used to evaluate whether the fault slip occurs, as shown in eq 19

$$|\tau| = \tau_0 + \mu\sigma_n \tag{19}$$

where τ is the shear stress on the fault plane, Pa; τ_0 is the inherent shear strength, Pa; and μ is the internal friction coefficient.

The normal stress and shear stress on the fault plane can be obtained using the Mohr circle method and expressed as[12]

$$\begin{cases} \sigma_n = \dfrac{(\sigma_1 + \sigma_3)}{2} + \dfrac{(\sigma_1 - \sigma_3)}{2}\cos 2\beta \\ |\tau| = \left|\dfrac{(\sigma_1 - \sigma_3)}{2}\sin 2\beta\right| \end{cases} \tag{20}$$

where σ_1 and σ_3 are the maximum and minimum principal stresses, Pa, respectively, and β is the dip angle of the fault, °.

Considering the changes of pore pressure and thermal stress caused by cold water injection in the fault, the normal stress and shear stress on the fault surface can be rewritten in the form of effective stress, as shown in eqs 21 and 22[10]

$$\begin{aligned} \sigma_n' &= \frac{(\sigma_1' + \sigma_3')}{2} + \frac{(\sigma_1' - \sigma_3')}{2}\cos 2\beta \\ &= \frac{(\sigma_1 - P_p - \sigma_T) + (\sigma_3 - P_p + \sigma_T)}{2} \\ &\quad + \frac{(\sigma_1 - P_p - \sigma_T) - (\sigma_3 - P_p - \sigma_T)}{2}\cos 2\beta \\ &= \sigma_n - P_p - \sigma_T \end{aligned} \tag{21}$$

$$\begin{aligned} |\tau'| &= \left|\frac{(\sigma_1' - \sigma_3')}{2}\sin 2\beta\right| \\ &= \left|\frac{(\sigma_1 - P_p - \sigma_T) - (\sigma_3 - P_p - \sigma_T)}{2}\sin 2\beta\right| = |\tau| \end{aligned} \tag{22}$$

where σ_n' and τ' are the effective normal and shear stress on the fault plane, Pa, respectively, and σ_n' and σ_3' are the maximum and minimum effective principal stresses, respectively, Pa.

Equations 21 and 22 show that pore pressure and thermal stress only affect the effective normal stress on the fault plane, while the effective shear stress is not affected. According to Coulomb's failure criterion, the Mohr circle is drawn as shown in Figure 2.

It can be seen that when the pore pressure increases, the effective normal stress decreases and the effective shear stress remains unchanged; then, the Mohr circle moves to the left. When the temperature decreases and the rock shrinks, the thermal stress becomes tensile stress, which will cause the effective normal stress to continue to decrease and the effective shear stress to remain unchanged, and the Mohr circle continues to move to the left. It can be seen that fault slip occurs due to the joint effect of increased pore pressure and decreased temperature. If the molar circle left shift caused by increased pore pressure and the molar circle left shift caused by decreased temperature reach the failure line after superposition, a shear slip will occur on the fault. If the effective stress continues to decrease and the Mohr circle continues to move to the left and completely crosses the fault failure line, the activation state of the fault will change to tensile failure.

Combined with the above-mentioned analysis results, eqs 21 and 22 can be substituted into eq 19 to obtain the calculation formula of FSP (fault slip potential)

$$\begin{aligned} \mathrm{FSP} &= \frac{|\tau'|}{\tau_0 + \mu\sigma_n'} \\ &= \frac{(\sigma_1 - \sigma_3)\sin 2\beta}{2\tau_0 + \mu[(\sigma_1 + \sigma_3) + (\sigma_1 - \sigma_3)\cos 2\beta - 2P_p - 2\sigma_T]} \end{aligned} \tag{23}$$

When considering the occurrence of different faults, the angle between the strike of any fault and the initial maximum horizontal in situ stress direction is α and the dip angle of the

https://doi.org/10.1021/acsomega.2c08111
ACS Omega 2023, 8, 8078−8091

fault is β. At this time, the principal stress direction on the fault plane is no longer consistent with that in the reservoir, as shown in Figure 3.[27]

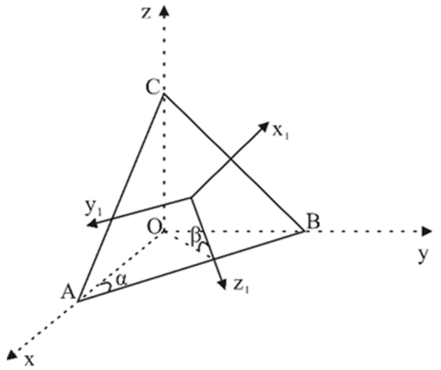

Figure 3. Schematics of the reservoir coordinates (x, y, z) and the fault coordinates (x_1, y_1, z_1).

After conversion from reservoir coordinates (x, y, z) to fault coordinates (x_1, y_1, z_1), the formula for calculating the normal stress on the fault plane can be rewritten as

$$\begin{cases} \sigma_n = \sigma_2 \cos^2(x_1, x) + \sigma_3 \cos^2(x_1, y) + \sigma_1 \cos^2(x_1, z) \\ \tau_{x_1y_1} = \sigma_2 \cos(x_1, x)\cos(y_1, x) + \sigma_3 \cos(x_1, y)\cos(y_1, y) \\ \qquad + \sigma_1 \cos(x_1, z)\cos(y_1, z) \\ \tau_{x_1z_1} = \sigma_2 \cos(x_1, x)\cos(z_1, x) + \sigma_3 \cos(x_1, y)\cos(z_1, y) \\ \qquad + \sigma_1 \cos(x_1, z)\cos(z_1, z) \end{cases} \tag{24}$$

The direction cosine in the above-mentioned equation can be obtained by eq 25

$$\begin{cases} \cos(x_1, x) = \sin\beta \sin\alpha;\ \cos(x_1, y) \\ \qquad = \sin\beta \cos\alpha;\ \cos(x_1, z) \\ \qquad = \cos\beta \\ \cos(y_1, x) = \cos\alpha;\ \cos(y_1, y) = -\sin\alpha;\ \cos(y_1, z) = 0 \\ \cos(z_1, x) = \cos\beta \sin\alpha;\ \cos(z_1, y) \\ \qquad = \cos\beta \cos\alpha;\ \cos(z_1, z) \\ \qquad = -\sin\beta \end{cases} \tag{25}$$

The effective normal stress and effective shear stress on the fault surface can be expressed as

$$\begin{cases} \sigma_n' = \sigma_n - P_p - \alpha_T \\ \tau_{x_1y_1}' = \tau_{x_1y_1} \\ \tau_{x_1z_1}' = \tau_{x_1z_1} \end{cases} \tag{26}$$

Equation 26 can be substituted into eq 19 to obtain the calculation equation of FSP under different occurrences

$$\mathrm{FSP} = \frac{|\tau'|}{\tau_0 + \mu\sigma_n'} = \frac{\sqrt{(\tau_{x_1y_1})^2 + (\tau_{x_1s_1})^2}}{\tau_0 + \mu(\sigma_n - P_\mathrm{P} - \alpha_\mathrm{T})} \tag{27}$$

According to the definition of the FSP, the following relationship can be used to determine the fault slips:

- FSP < 1: the fault is in a stable state and will not slip.
- FSP = 1: the fault is in the critical state of activation and is about to slip.
- FSP > 1: the fault is in an unstable state and slips.

3. NUMERICAL SIMULATION MODEL

Since the hot dry rock reservoir is mostly granite with very low permeability, it is necessary to transform the hot dry rock reservoir to form a fracture network during the development of hot dry rock. This production mode is called EGS (enhanced geothermal system). This paper only studies the distribution of the temperature field, seepage field, and strain field in the development process of hot dry rock. For the purpose of saving computing resources, it is assumed that the hot dry rock reservoir is still uniform continuous medium after transformation, and the transformation only improves the overall average permeability of the hot dry rock reservoir. In addition, in the process of hot dry rock injection−production simulation, only the behavior of the hot dry rock reservoir is considered and the upper and lower cap layers are ignored. Figure 4 shows the geometric diagram of the hot dry rock

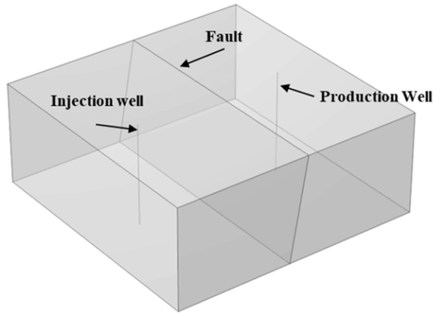

Figure 4. Schematic diagram of the numerical simulation model.

injection−production model. It is assumed that the top of the reservoir is located 3300 m deep underground, the thickness of the reservoir is 200 m, the length and width are 500 m, and there is a fault with an angle of 0° between the strike and the maximum horizontal in situ stress direction and a dip angle of 80° in the reservoir. The two cylinders in the figure represent the injection well and the production well, and the distance and arrangement between the injection well and the production well are set according to different simulation conditions.

In this study, the values of the properties of the hot dry rock reservoir are listed in Table 1.

The initial pore pressure of the model is 10 MPa, and the initial temperature is 200 °C. The outer boundaries of the model are impervious boundaries and thermal insulation boundaries. The vertical ground stress is 70 MPa, the maximum horizontal ground stress is 55 MPa, and the minimum horizontal ground stress is 50 MPa. The injection well is filled with cold water at a constant flow rate at a temperature of 20 °C. The production well has a constant production bottom hole pressure of 10 MPa, and no temperature boundary is set. Equation 28 is the equation for calculating the mass flow of the injected water in the injection well, and eq 29 is the equation for calculating the heat source term caused by the injected water.

https://doi.org/10.1021/acsomega.2c08111
ACS Omega 2023, 8, 8078−8091

Table 1. Computational Parameters of the Hot Dry Rock Reservoir

parameter	value	units
elasticity modulus	30×10^9	Pa
Poissons ratio	0.16	
initial permeability	5×10^{-15}	m^2
initial porosity	0.01	
thermal conductivity of rock	3	W/(m·°C)
density of rock	2600	kg/m^3
specific heat capacity of rock	990	J/(kg·°C)
thermal conductivity of water	1.5	W/(m·°C)
initial density of water	1000	kg/m^3
specific heat capacity of water	4200	J/(kg·°C)
thermal expansion coefficient	1.2×10^{-6}	1/°C
Biot coefficient	1	

$$M_0 = Q_{inj}\rho_l \tag{28}$$

$$Q = C_{p,l}\frac{M_0}{l}(T_{inj} - T) \tag{29}$$

Figure 5a shows the pore pressure distribution of the reservoir at 25, 50, and 100 years of production. At 25 years of production, the cold zone inside the reservoir was blue fusiform. At the 50th year of production, the area of low temperature continued to increase but at a lower rate than in the first 25 years. At 100 years of production, with 300 m injection−production well spacing, the blue zone has spread throughout the reservoir. Figure 5b shows the reservoir temperature distribution at 25, 50, and 100 years of production. It can be seen that with the increase of production time, the overall pore pressure in the reservoir also increases, and the increase is most obvious near the injection well, reaching a maximum of 39.7 MPa. Figure 5c shows the temperature distribution of the reservoir at 25, 50, and 100 years of production. It can be seen that the volume strain of the reservoir rock is affected by both pore pressure and thermal stress. In the early stage of injection and production, the volume strain in the low-temperature area is negative, while the volume strain in the high-temperature area is positive, which indicates that the volume strain caused by the temperature change in the low-temperature area is greater than that caused by the increase of pore pressure, and the temperature change is dominant at this time. However, as the production time continues to increase, the volume strain in the low-temperature region becomes positive, and combined with the pore pressure change, it can be seen that the pore pressure change is dominant at this time.

4. RESULTS AND DISCUSSION

4.1. Influence of Different Injection−Production Well Spacings. Figure 6a shows the variation of thermal stress on the fault surface with time under different injection−production well spacings. It is clear that as the well spacing increases the distance between the injection well and the fault, the cold zone cannot reach the fault for a short period of time, and the thermal stress at the fault increases. When the thermal stress occurs at the fault, the increase rate of thermal stress increases with the increase of well spacing and finally flattens out until the temperature at the fault is equal to the temperature of injection water. Figure 6b shows the relationship between pore pressure and time on the fault surface at

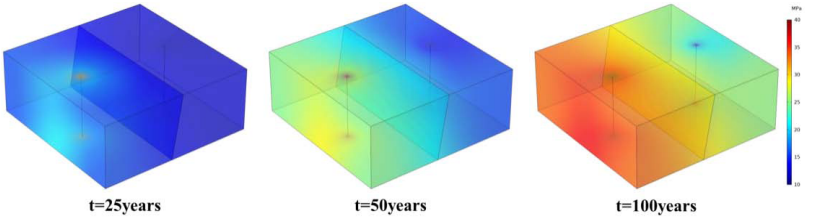

(a) Pore pressure distribution at different times

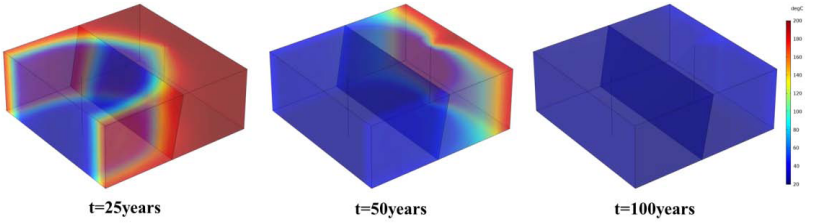

(b) Temperature distribution at different times

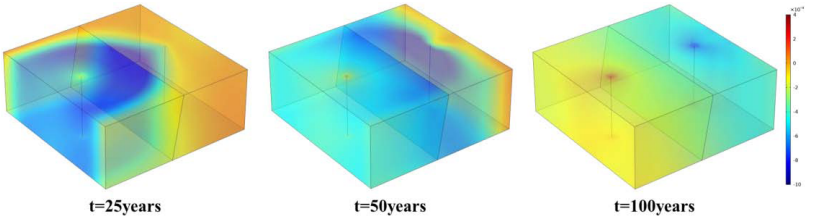

(c) Volumetric strain distribution at different times

Figure 5. Physical field distribution at different times.

https://doi.org/10.1021/acsomega.2c08111
ACS Omega 2023, 8, 8078−8091

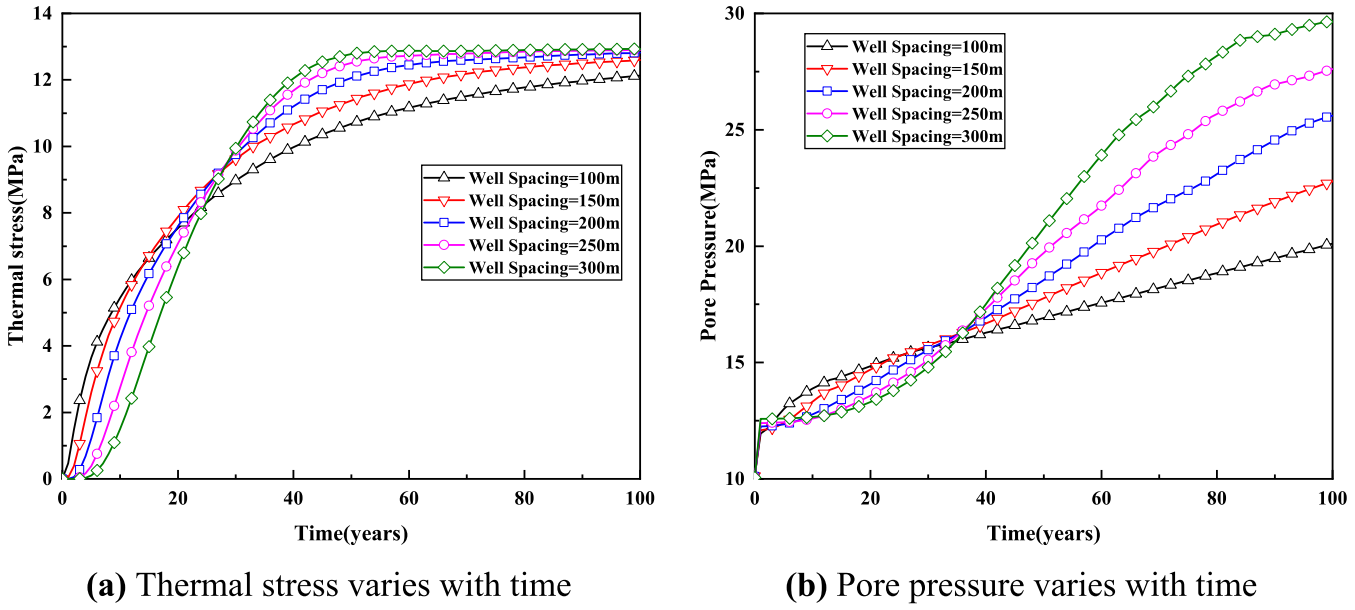

Figure 6. Variation of pore pressure and thermal stress in the fault plane at different injection−production well spacings.

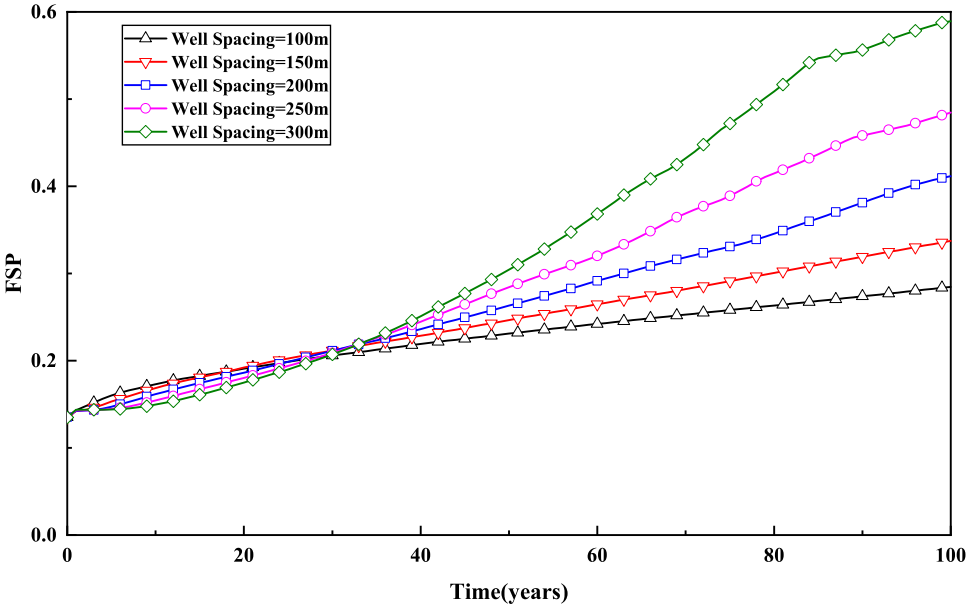

Figure 7. FSP changes with time at different injection−production spacings.

different well spacings. From the graph, we can see that in the production of first years, the pore pressure increases rapidly and the spacing is more enlarged with the pore pressure increase; this shows that the fluid injection changed the balance of the original formation of the seepage field; after pore pressure surge, there will be a period of stability, and the stability and the thermal stress under different well spacings are zero at the same time. With the increase of production time, the pore pressure increases slowly after the stable period, and the increasing rate increases with the increase of well spacing. According to the changes of thermal stress in fault layers at different well spacings, thermal stress also increases during the period of the pore pressure increase, which indicates that the decrease of reservoir temperature and the increase of thermal stress will lead to reservoir shrinkage deformation and then reduce permeability. After the decrease of permeability, the pore pressure in the reservoir increases. It is also verified that there is a very strong multifield coupling phenomenon in the process of the hot dry rock reservoir.

Figure 7 shows the change of fault activation risk with time under different injection and production well spacings, as can be seen from the figure: In the first 30 years of production, the increase of the FSP in the case of a small injection−production well spacing is greater than that in the case of a large injection−production well spacing. This is because the small injection−production well spacing allows the injected cryogenic fluid to reach the fault in a shorter time and generate additional heating stress near the fault faster. With the increase of production time, the value of the FSP increases with the increase of the well spacing and the value of the FSP increases faster with the increase of the injection−production well spacing. When the injection−production well spacing is 300 m,

https://doi.org/10.1021/acsomega.2c08111
ACS Omega 2023, 8, 8078−8091

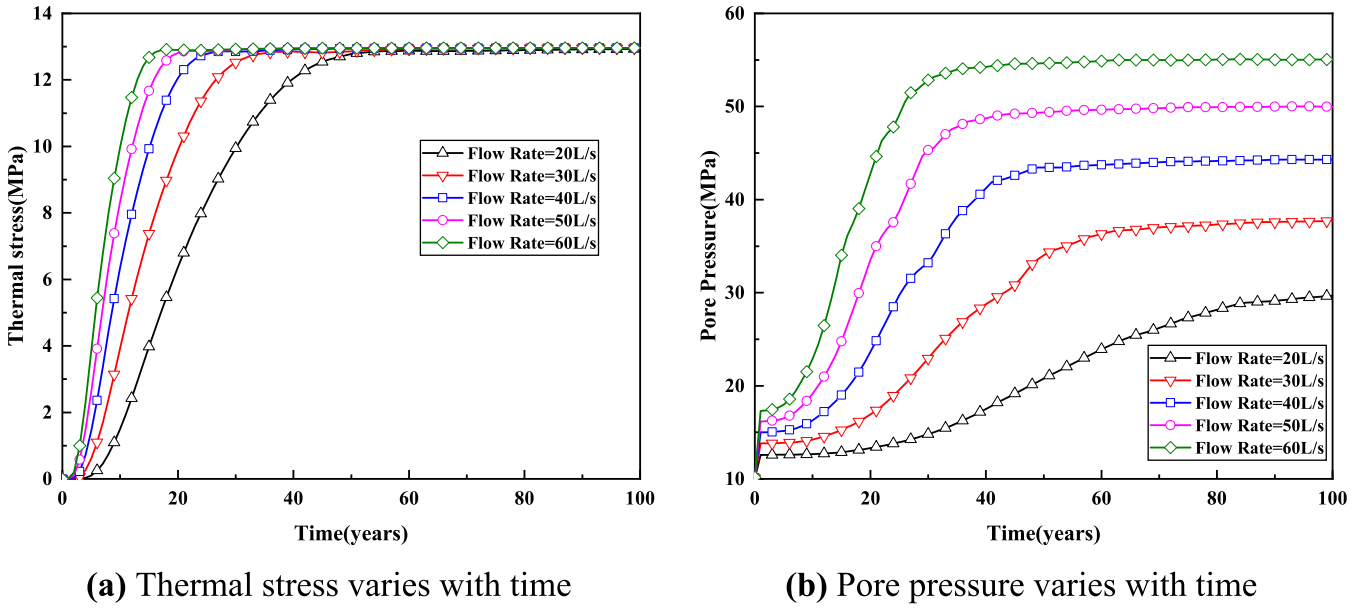

Figure 8. Variation of pore pressure and thermal stress in the fault plane with different injection flow rates.

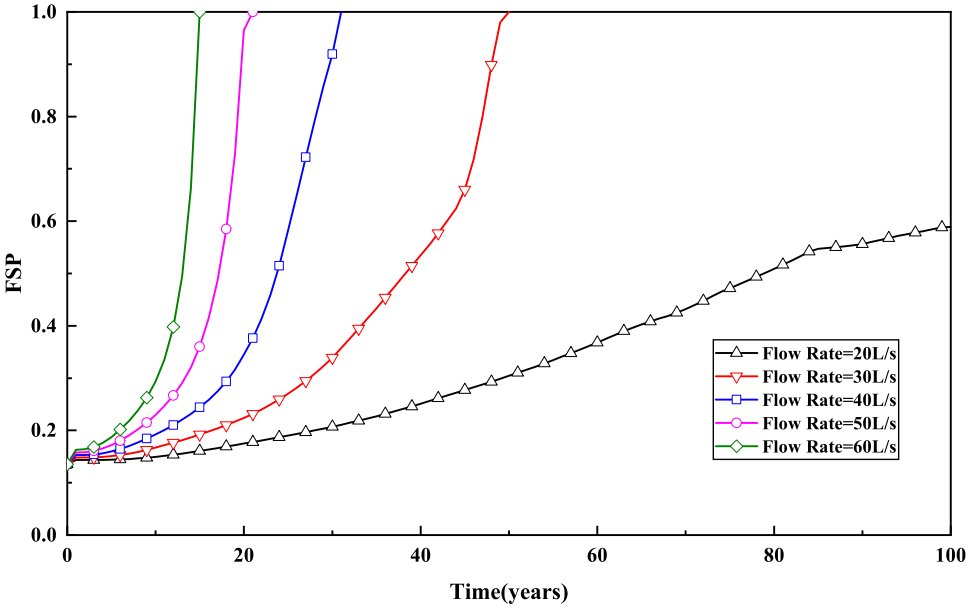

Figure 9. FSP changes with time at different injection flow rates.

the maximum value can reach 0.58. Although the FSP is less than 1 in the whole process, it can be seen from the variation of FSP under different injection−production well spacings that the greater the injection−production well spacing, the higher the risk of fault activation in long-term production.

4.2. Influence of Different Injection Flows. Figure 8a shows the time-varying relationship of thermal stress at the fault plane at different flow rates. It can be seen that the time of thermal stress at fracture is different with different flow rates. On the whole, the higher the injection flow rate, the shorter the time of thermal stress. In addition, with the increase of the injection flow rate, the thermal stress increases faster and the time to reach stability is shorter. This is because in the case of the same flow area, the larger the flow rate, the larger the velocity, and the shorter the time for the cryogenic fluid to reach the vicinity of the fault and the greater the flow rate, the more intense the heat exchange between the cryogenic fluid and the thermal reservoir, so the thermal stress increases faster. Figure 8b shows the variation of pore pressure in the fault plane with time under different injection flow rates. Under different injection flow rates, the original stable seepage field in the reservoir at the beginning of injection−production changes under the disturbance of the injection fluid. To restore the equilibrium of the seepage field, the pore pressure in the reservoir increases sharply, and the increase of the injection flow rate increases more. After the increase of pore pressure, since there is no thermal stress at the fault at this time, pore pressure will remain stable for a period of time, and the length of this period of stability is close to the period when the thermal stress is 0. After the stable period, pore pressure continues to increase as the reservoir shrinks during the heat transfer process and the permeability decreases, and the

https://doi.org/10.1021/acsomega.2c08111
ACS Omega 2023, 8, 8078−8091

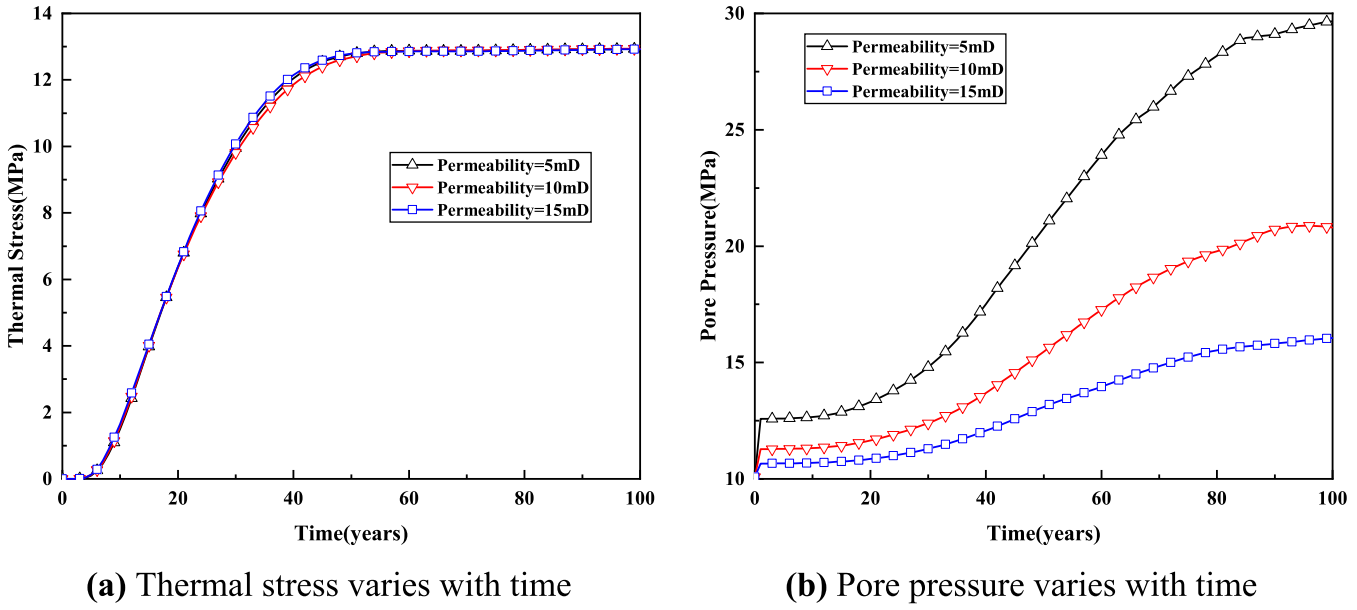

Figure 10. Variation of pore pressure and thermal stress in the fault plane at different permeabilities.

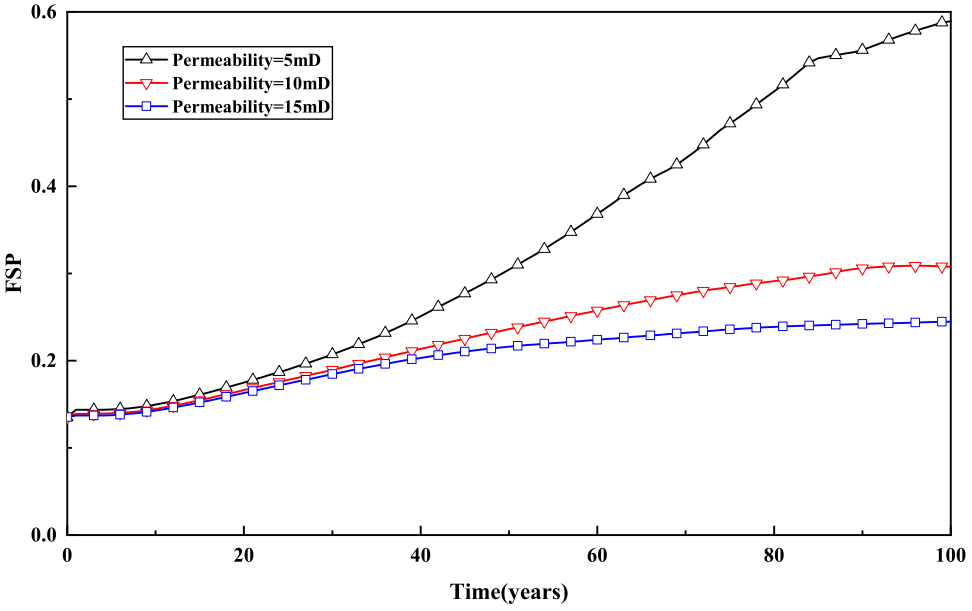

Figure 11. FSP changes with time at different permeabilities.

injection flow rate increases faster. Finally, the pore pressure value and stabilization time increase with the increase of the injection flow rate.

Figure 9 shows the variation of the FSP with the injection−production time at different injection flow rates. It can be seen that in the case of a small injection flow, the FSP value in the whole injection−production process shows an increasing trend but does not reach 1, indicating that there is no risk of fault activation in the whole injection−production process under the condition of small injection flow. However, with the increase of the injection flow rate, the increasing speed of the FSP increases and the time required for fault activation decreases with the increase of the injection flow rate.

4.3. Influence of Different Reservoir Permeabilities. Figure 10a shows the variation of thermal stress over time in fracture layers with different reservoir permeabilities. It can be seen that the variation of thermal stress at the fracture layer under different permeabilities is the same with time and the magnitude is almost the same. This is because the intensity of heat exchange between the injected fluid and the reservoir is mainly determined by the seepage velocity of the fluid under the condition that the injected fluid has the same property and the seepage velocity is also the same under the condition that the injected fluid has the same flow rate and the same flow area, so the heat recovery effect is basically the same under the three permeabilities. Figure 10b shows the variation of pore pressure at fault layers with different permeabilities over time. With the increase of time, pore pressure at fault layers with different permeabilities shows an increasing trend. As the thermal stress variation trend and size are consistent at different permeabilities, the variation trend of pore pressure is basically the same. In addition, according to Darcy's law, when

https://doi.org/10.1021/acsomega.2c08111
ACS Omega 2023, 8, 8078−8091

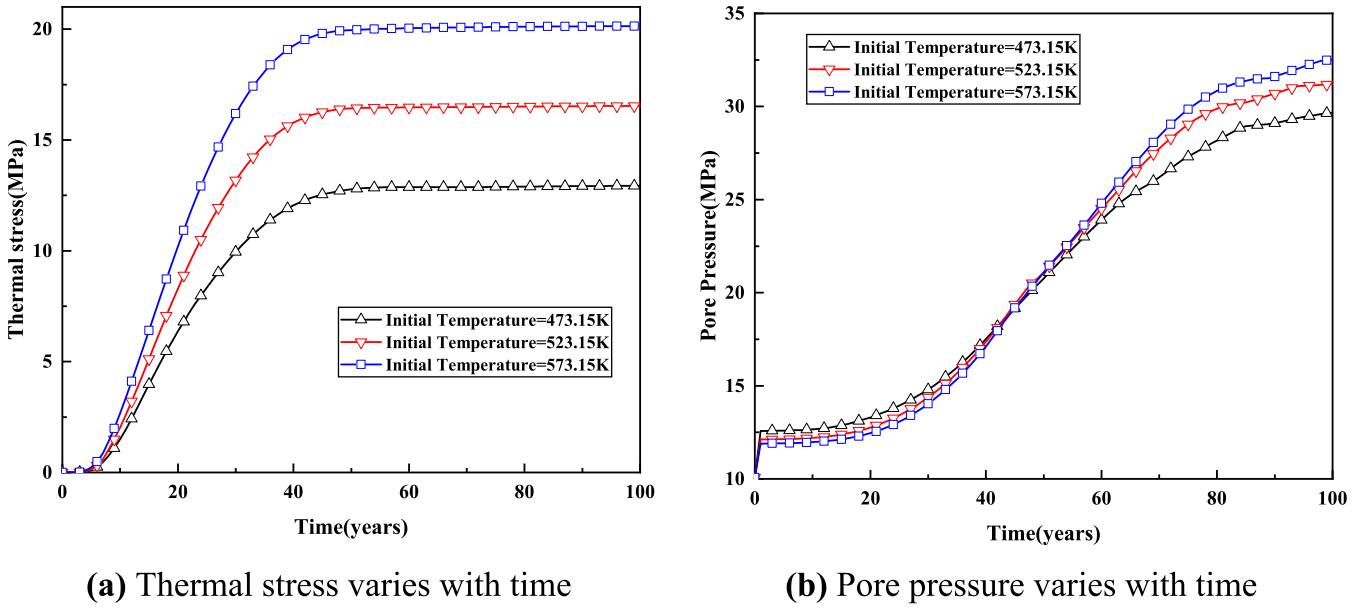

Figure 12. Variation of pore pressure and thermal stress in the fault plane at different initial reservoir temperatures.

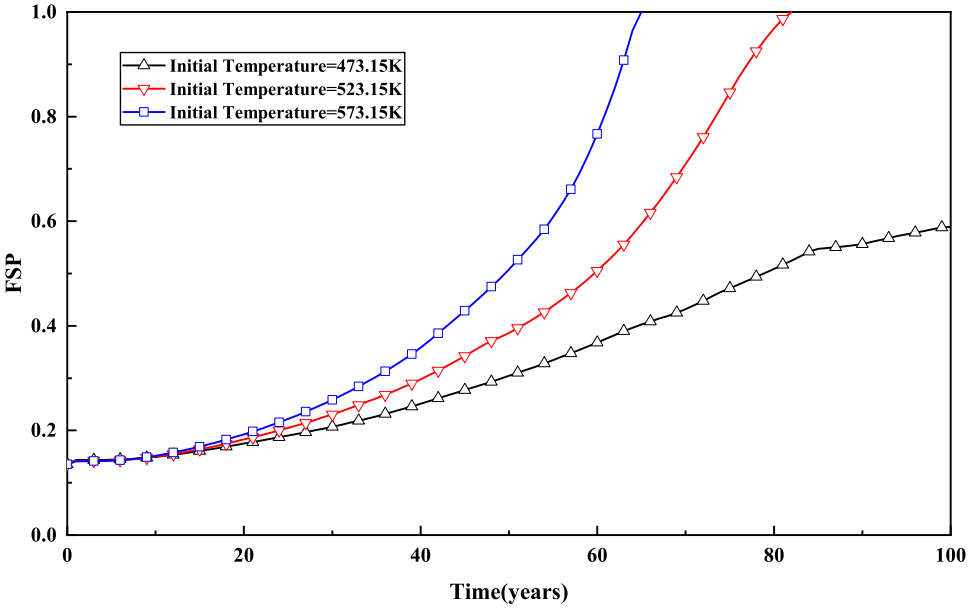

Figure 13. FSP changes with time at different injection flows.

the injected fluid has the same property and same flow rate, the lower the permeability, the greater the difference, so the lower the reservoir permeability, the higher the pore pressure at the same time.

Figure 11 shows the relationship between the FSP and injection−production time under different permeabilities. When the other conditions are the same, at same time, the greater the reservoir permeability in the process of injection−production, the smaller the FSP value, so in the hot dry rock reservoir renovation, we should try to increase the size of the overall hot dry rock reservoir permeability in the injection−production process to reduce the risk of fault activation. In addition, the variation pattern of the FSP with time under different permeabilities is similar to that of pore pressure, indicating that the variation of pore pressure under different permeabilities plays a major role in the risk of fault activation.

4.4. Influence of the Initial Temperature of Different Reservoirs. Under the same injection and production conditions and different initial reservoir temperatures, the variation of thermal stress at the fault plane with time is shown in Figure 12a; it can be seen that with the increase of the initial reservoir temperature, the injection of cold water into the reservoir results in increased thermal stress at the fault, but due to the injection of cold water, the flow rate and injection−production well spacing are the same; as a result, the thermal stress changes in the fault strata at different initial temperatures are the same, but the size is different. Figure 12b shows the relationship between pore pressure at the fault plane and time at different initial temperatures. It can be seen that the pore pressure at the fault layer decreases with the increase of the initial reservoir temperature in the early production period but

https://doi.org/10.1021/acsomega.2c08111
ACS Omega 2023, 8, 8078−8091

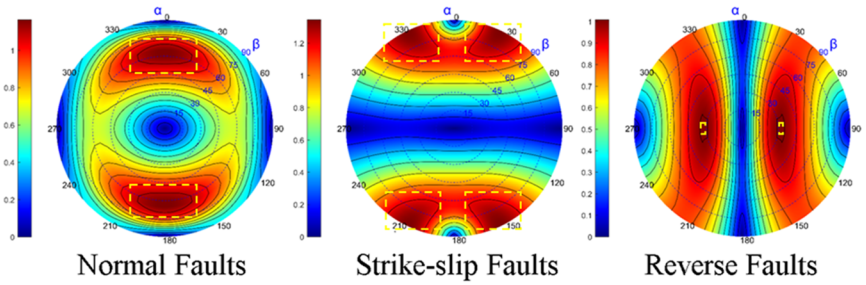

(a) FSP changes under different fault occurrences

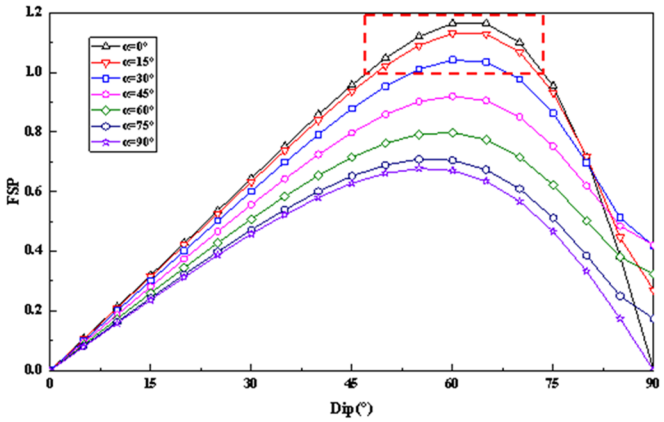

(b) FSP changes with fault occurrence under normal fault mechanism

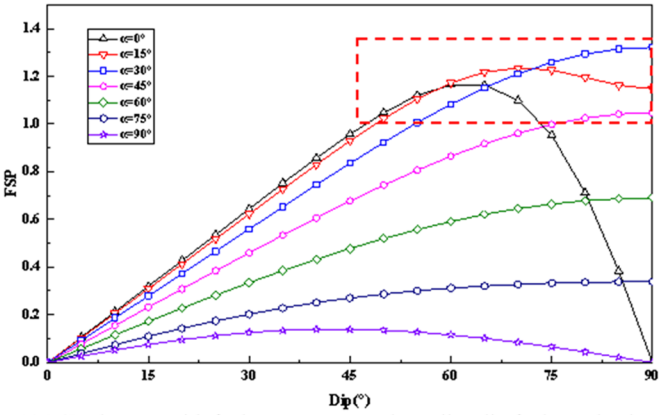

(c) FSP changes with fault occurrence under strike-slip fault mechanism

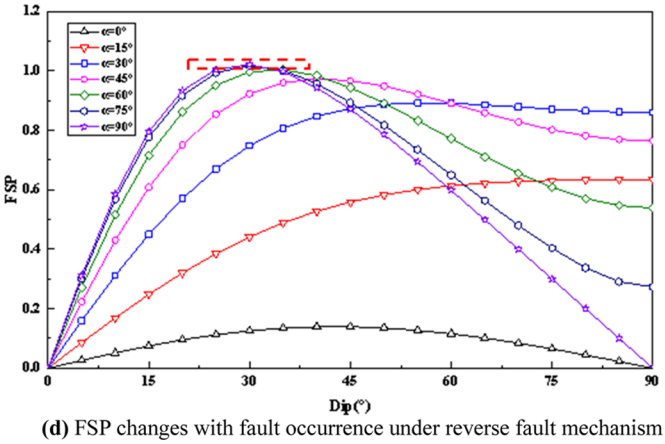

(d) FSP changes with fault occurrence under reverse fault mechanism

Figure 14. FSP changes under different fault occurrences.

increases with the increase of the initial reservoir temperature in the late production period.

Figure 13 shows the the time-varying relationship of the FSP at different initial reservoir temperatures. It can be seen that the FSP does not change significantly at different initial

https://doi.org/10.1021/acsomega.2c08111
ACS Omega 2023, 8, 8078−8091

reservoir temperatures in early production, which also indicates that the risk of fault activation is basically the same at different initial reservoir temperatures in early production. However, the FSP value increases with the increase of initial reservoir temperatures in late production, leading to an increase in the fault activation risk. Therefore, in the development of hot dry rock reservoirs with a high initial reservoir temperature, the injection flow rate, injection water temperature, and other engineering parameters should be controlled in the later production period to avoid fault activation caused when using the same or similar engineering parameters with a lower initial temperature.

4.5. Influence of Different Fault Occurrences. Figure 14 shows the variation rule of the FSP with fault occurrence under different fault occurrences. As Figure 14a is highly symmetric, the range of 1/4 is taken for analysis. In Figure 14b–d, the horizontal axis is the fault dip angle and the vertical axis is the FSP. Each curve shows the variation rule of the FSP with the fault dip angle under different fault strikes and the maximum horizontal ground stress direction, respectively. The fault activation sections are clearly marked with a dashed rectangle in Figure 14.

Figure 14b shows the variation of the FSP with fault occurrence under normal fault mechanisms. It can be seen that FSP increases first and then decreases with the increase of the dip angle of the fault and reaches its maximum value when the dip angle of the fault is between 55 and 65°. In addition, the FSP decreases gradually with the increase of the angle between the fault strike and the direction of the maximum horizontal in situ stress. When the fault strike is parallel to the direction of the maximum horizontal in situ stress, the FSP is the largest and the risk of fault activation is also greater. According to the above-mentioned rules, the following suggestions are given: when the strike of the fault is parallel to the horizontal maximum ground stress and the dip angle of the fault is between 55° and 65°, the injection flow should be strictly controlled during the hot dry rock injection and production; otherwise, the fault activation will occur.

Figure 14c shows the variation of the FSP with the fault occurrence under the strike-slip fault mechanism. When the angle between the fault strike and the direction of the maximum horizontal in situ stress is 0, 15, and 90°, the FSP increases first and then decreases with the increase of the dip angle. The difference is that when the angle between the fault strike and the direction of the maximum horizontal in situ stress is 0°, the FSP is greater than 1 in the range of the dip angle between 50 and 70°. When the angle between the fault strike and the direction of the maximum horizontal in situ stress is 15°, the FSP is greater than 1 in the range of the fault dip angle from 50 to 90°. When the angle between the fault strike and the direction of the maximum horizontal in situ stress is 90°, the FSP is always less than 1. When the angle between the fault strike and the direction of the maximum horizontal in situ stress is between 30 and 75°, the FSP increases with the increase of the fault dip angle. Especially, when the angle between the fault strike and the direction of the maximum horizontal in situ stress is between 30° and 45° and the fault dip angle is greater than 55°, the FSP is greater than 1. According to the above-mentioned rules, the fault activation risk can be summarized as follows: When the fault dip angle is small, the fault does not have activation risk regardless of the angle between the fault strike and the direction of the maximum horizontal in situ stress. However, with the increase of the fault dip angle, the smaller the angle between the fault strike and the fault, the more likely it is to be activated. Therefore, attention should be paid to the injection and production of hot dry rock when strike-slip faults exist in the reservoir. The injection flow rate should be strictly controlled when the fault dip angle is large and the angle between the fault strike and the direction of maximum horizontal in situ stress is small, so as to avoid the risk of fault activation.

Figure 14d shows the variation of the FSP with fault occurrence under the reverse fault mechanism. It can be seen that when the angle between the fault strike and the direction of the maximum horizontal in situ stress is 15°, the FSP increases first and then becomes stable, and its maximum value is less than 1. In other cases, the FSP increases first and then decreases. When the angle between the fault strike and the direction of the maximum horizontal in situ stress is 90°, the FSP is greater than 1 when the fault dip angle is between 20 and 25°. When the angle between the fault strike and the direction of the maximum horizontal in situ stress is 75°, the FSP is greater than 1 when the fault dip angle is between 30 and 35°. In other cases, the FSP value is less than 1. It can be seen that the greater the angle between the fault strike and the direction of the maximum horizontal in situ stress, the more likely the fault activation is under the condition of a smaller dip angle. According to the above-mentioned changes, the following suggestions can be given for the injection and production of hot dry rock in the case of reverse faults in the reservoir: when the angle between the fault strike and the direction of the maximum horizontal in situ stress is large and the fault dip angle is small, the injection flow rate should be strictly controlled to reduce the risk of fault activation.

5. CONCLUSIONS

(1) The stress state at the fault layer is affected by the comprehensive action of pore pressure and thermal stress at the fault layer. Under different conditions, the variation of thermal stress and pore pressure leads to the different distributions of stress states at the fault layer.
(2) Under the same geological conditions, the risk of fault activation increases with the increase of the injection–production well spacing and injection flow rate.
(3) Under the same injection–production conditions, the lower the reservoir permeability, the greater the fault activation risk and the higher the initial reservoir temperature, the greater the fault activation risk.
(4) When normal faults exist in the reservoir, the fault activation risk is maximum when the angle between the fault strike and the direction of the maximum horizontal in situ stress is 0°. When strike-slip faults are in the reservoir, the fault activation risk is larger when the angle between the fault strike and the direction of the maximum horizontal in situ stress is small and the fault dip angle is large. When reverse faults exist in the reservoir, the fault activation risk is larger when the angle between the fault strike and the direction of the maximum horizontal in situ stress is larger and the fault dip angle is smaller.

AUTHOR INFORMATION

Corresponding Author

Kai Zhao – *College of Petroleum Engineering, Xi'an Shiyou University, Xi'an 710065, China; State Key Laboratory of*

https://doi.org/10.1021/acsomega.2c08111
ACS Omega 2023, 8, 8078–8091

Oil and Gas Reservoir Geology and Exploitation, Chengdu University of Technology, Chengdu 610059, China; orcid.org/0000-0002-0170-8532; Email: zkaiup@126.com

Authors

Xiaoyun Wang − *College of Petroleum Engineering, Xi'an Shiyou University, Xi'an 710065, China*

Yongcun Feng − *College of Petroleum Engineering, China University of Petroleum (Beijing), Beijing 102249, China*

Wei Gao − *College of Petroleum Engineering, Xi'an Shiyou University, Xi'an 710065, China*

Wenjie Song − *College of Petroleum Engineering, Xi'an Shiyou University, Xi'an 710065, China*

Liangbin Dou − *College of Petroleum Engineering, Xi'an Shiyou University, Xi'an 710065, China*

Hailong Jiang − *College of Petroleum Engineering, Xi'an Shiyou University, Xi'an 710065, China*

Complete contact information is available at: https://pubs.acs.org/10.1021/acsomega.2c08111

Notes

The authors declare no competing financial interest.

■ ACKNOWLEDGMENTS

This work might not be possible without the financial support from the National Natural Science Foundation of China (Nos. 52074224, 52074221, 52104005), the Key Research and Development Program of Shaanxi Province (grant number 2023-YBGY-312), the Open Fund (PLC2020048) of State Key Laboratory of Oil and Gas Reservoir Geology and Exploitation(Chengdu University of Technology), and the Postgraduate Innovation and Practice Ability Development Fund of Xi'an Shiyou University (grant number YCS22211002).

■ NOMENCLATURES

$\sigma_{ji,j}$stress tensor component, Pa;
ε_{ij}strain tensor component;
$\mu_{i,j}$displacement vector, m;
$G = E/2\ (1 + \nu)$modulus of rigidity, Pa;
$\lambda = \frac{E\nu}{(1+\nu)(1-2\nu)}$Lame's parameters, Pa;
Eelastic modulus of rock matrix, Pa;
νPoisson's ratio of the rock;
$\varepsilon_v$volume strain of the rock;
Kbulk elastic modulus, Pa;
$\alpha_T$thermal expansion coefficient of rock, 1/K;
Treservoir temperature, K;
T_0initial reservoir temperature, K;
α_pBiot coefficient;
$p$pore pressure, Pa;
$p_0$initial pore pressure, Pa;
δ_{ij}Kronecker delta;
$\rho_l$density of the injected fluid density, kg/m^3;
$v$velocity of fluid flow,m/s;
$v_r$relative velocity of the fluid flow, m/s;
ϕporosity of the rock;
$k$permeability of the rock, m^2;
μviscosity of the injected fluid, Pa·s;
$v_s$viscosity of the rock, m/s;
ρ_{l0}initial density of the injected fluid, kg/m^3;
$c_l$pressure coefficient of the injected fluid, 1/Pa;
$\beta_l$temperature coefficient of the injected fluid, 1/K;
$q$heat flux, J/(s·m^2);
λthermal conductivity of the rock, W/(m·K);
$c_s$specific heat capacity of the rock, J/(kg·°C);
$\rho_s$density of the rock, kg/m^3;
$c_f$specific heat capacity of the injected fluid, J/(kg·°C);
τshear stress on the fault plane, Pa;
$\tau_0$inherent shear strength, Pa;
μinternal friction coefficient;
σ_n' and τ'effective normal and shear stress on the fault plane, respectively, Pa;
σ_1' and σ_3'maximum and minimum effective principal stresses, respectively, Pa;

■ REFERENCES

(1) Anderson, A.; Rezaie, B. Geothermal technology: Trends and potential role in a sustainable future. *Appl. Energy* **2019**, *248*, 18−34.
(2) Melikoglu, M. Geothermal energy in Turkey and around the World: A review of the literature and an analysis based on Turkey's Vision 2023 energy targets. *Renewable Sustainable Energy Rev.* **2017**, *76*, 485−492.
(3) Barbier, E. Geothermal energy technology and current status: an overview. *Renewable Sustainable Energy Rev.* **2002**, *6*, 3−65.
(4) Di Fraia, S.; Macaluso, A.; Massarotti, N.; Vanoli, L. Energy, exergy and economic analysis 'of a novel geothermal energy system for wastewater and sludge treatment. *Energy Convers. Manage.* **2019**, *195*, 533−547.
(5) Olasolo, P.; Juárez, M-C.; Olasolo, J.; Morales, M. P.; Valdani, D. Economic analysis of Enhanced Geothermal Systems (EGS). A review of software packages for estimating and simulating costs. *Appl. Therm. Eng.* **2016**, *104*, 104647−104658.
(6) Yeo, I.-W.; Brown, M. R. M.; Ge, S.; Lee, K. K. Causal mechanism of injection-induced earthquakes through the Mw 5.5 Pohang earthquake case study. *Nat. Commun.* **2020**, *11*, No. 2614.
(7) Kwiatek, G.; Saarno, T.; Ader, T.; Bluemle, F.; Bohnhoff, M.; Chendorain, M.; Dresen, G.; Heikkinen, P.; Kukkonen, I.; Leary, P.; Leonhardt, M.; Malin, P.; Martínez-Garzón, P.; Passmore, K.; Passmore, P.; Valenzuela, S.; Wollin, C. Controlling fluid-induced seismicity during a 6.1-km-deep geothermal stimulation in Finland. *Sci. Adv.* **2019**, *5*, eaav7224.
(8) Ellsworth, W.-L.; Giardini, D.; Townend, J.; Ge, S.; Shimamoto, T. Triggering of the Pohang, Korea, Earthquake (Mw 5.5) by Enhanced Geothermal System Stimulation. *Seismological Res. Lett.* **2019**, *90*, 1844−1858.
(9) Yin, X.; Jiang, C.; Zhai, H.; Zhang, Y.; Jiang, C.; Lai, G.; Zhu, A.; Yin, F. Review of induced seismicity and disaster risk control in dry hot rock resource development worldwide. *Chin. J. Geophys.* **2021**, *64*, 3817−3836.
(10) Chen, Z.; Jingen, D.; Baohua, Y.; Zhang, Y.; Chen, Z. Estimation of upper limit of pore pressure by fault stability analysis. *J. Geophys. Eng.* **2016**, *13*, 313−319.
(11) Breede, K.; Dzebisashvili, K.; Liu, X.; Falcone, G. A systematic review of enhanced (or engineered) geothermal systems: past, present and future. *Geotherm. Energy* **2013**, *1*, 4.
(12) King hubbert, M.; Rubey, W.-W. Role of Fluid Pressure in Mechanics of Overthrust Faulting. *Geol. Soc. Am. Bull.* **1959**, *70*, 115.
(13) Raleigh, C.-B.; Healy, J.-H.; Bredehoeft, J.-D. An Experiment in Earthquake Control at Rangely, Colorado. *Science* **1976**, *191*, 1230−1237.
(14) Yerkes, R.-F.; Castle, R.-O. Seismicity and faulting attributable to fluid extraction. *Eng. Geol.* **1976**, *10*, 151−167.
(15) Nicholson, C.; Roeloffs, E.; Wesson, R.-L. The northeastern Ohio earthquake of 31 January 1986: Was it induced? *Bull. Seismol. Soc. Am.* **1988**, 188−217.
(16) Grasso, J.-R. Mechanics of seismic instabilities induced by the recovery of hydrocarbons. *Pure Appl. Geophys. PAGEOPH* **1992**, *139*, 507−534.

(17) Segall, P.; Fitzgerald, S. D. A note on induced stress changes in hydrocarbon and geothermal reservoirs. *Tectonophysics* **1998**, *289*, 117−128.
(18) Castillo, D.-A.; Bishop, D.-J.; Donaldson, I.; Kuek, D.; de Ruig, M.; Trupp, M.; Shuster, M. W. Anonymous. Trap integrity in the Laminaria High-Nancar Trough region, Timor Sea: Prediction of fault seal failure using well-constrained stress tensors and fault surfaces interpreted from 3D seismic. *APPEA J.* **2000**, *40*, 151.
(19) Wiprut, D.; Zoback, M.-D. Fault reactivation and fluid flow along a previously dormant normal fault in the Northern North Sea. *Geology* **2000**, *28*, 595−598.
(20) Evans, K. F.; Zappone, A.; Kraft, T.; Deichmann, N.; Moia, F. A survey of the induced seismic responses to fluid injection in geothermal and CO2 reservoirs in Europe. *Geothermics* **2012**, *41*, 30−54.
(21) Zoback, M. D.; Gorelick, S. M. Earthquake triggering and large-scale geologic storage of carbon dioxide. *Proc. Natl. Acad. Sci. U.S.A.* **2012**, *109*, 10164−10168.
(22) Zhao, K.; Li, X.; Yan, C.; Feng, Y.; Dou, L.; Li, J. A New Approach To Evaluate Fault-Sliding Potential With Reservoir Depletion. *SPE J.* **2019**, *24*, 2320−2334.
(23) McGarr, A. Maximum magnitude earthquakes induced by fluid injection(Article). *J. Geophys. Res.: Solid Earth* **2014**, *119*, 1008−1019.
(24) Ellsworth, W. L. Injection-Induced Earthquakes *Science* 2013, *341*6142 DOI: 10.1126/science.1225942.
(25) Zhao, Y.; Feng, Z.; Feng, Z.; Yang, D.; Liang, W. THM (Thermo-hydro-mechanical) coupled mathematical model of fractured media and numerical simulation of a 3D enhanced geothermal system at 573 K and buried depth 6000−7000 M. *Energy* **2015**, *82*, 193−205.
(26) Sun, Z.-x.; Xu, Z.; Yi, X.; Jun, Y.; Hao-xuan, W.; Shuhuan, L.; Zhi-lei, S.; Yong, H.; Ming-yu, C.; Xiaoxue, H. Numerical simulation of the heat extraction in EGS with thermal-hydraulic-mechanical coupling method based on discrete fractures model. *Energy* **2017**, *120*, 20−33.
(27) Junsheng, W. K. D. A quantitative relationship between the crustal stress and fault sealing ability. *Acta Pet. Sin.* **2012**, *33*, 74−81.

https://doi.org/10.1021/acsomega.2c08111
ACS Omega 2023, 8, 8078−8091